Acta Crystallographica Section D
**Biological Crystallography**
ISSN 0907-4449

# Photoreduction of the active site of the metalloprotein putidaredoxin by synchrotron radiation

**Mary C. Corbett,[a] Matthew J. Latimer,[b] Thomas L. Poulos,[c,d] Irina F. Sevrioukova,[c] Keith O. Hodgson[a,b]* and Britt Hedman[b]***

[a]Department of Chemistry, Stanford University, Stanford, CA 94305-5080, USA, [b]Stanford Synchrotron Radiation Laboratory, SLAC, Stanford University, 2575 Sand Hill Road, MS 69, Menlo Park, CA 94025-7015, USA, [c]Departments of Molecular Biology and Biochemistry, University of California, Irvine, CA 92697-3900, USA, and [d]Departments of Physiology and Biophysics and Chemistry, University of California, Irvine, CA 92697-3900, USA

Correspondence e-mail: hodgson@ssrl.slac.stanford.edu, hedman@ssrl.slac.stanford.edu

Received 24 April 2007
Accepted 18 July 2007

X-ray damage to protein crystals is often assessed on the basis of the degradation of diffraction intensity, yet this measure is not sensitive to the rapid changes that occur at photosensitive groups such as the active sites of metalloproteins. Here, X-ray absorption spectroscopy is used to study the X-ray dose-dependent photoreduction of crystals of the $[Fe_2S_2]$-containing metalloprotein putidaredoxin. A dramatic decrease in the rate of photoreduction is observed in crystals cryocooled with liquid helium at 40 K compared with those cooled with liquid nitrogen at 110 K. Whereas structural changes consistent with cluster reduction occur in the active site of the crystal measured at 110 K, no such changes occur in the crystal measured at 40 K, even after an eightfold increase in dose. When the structural results from extended X-ray absorption fine-structure measurements are compared with those obtained by crystallography on this and similar proteins, it is apparent that X-ray-induced photoreduction has had an impact on the crystallographic data and subsequent structure solutions. These results strongly indicate the importance of using liquid-helium-based cooling for metalloprotein crystallography in order to avoid the subtle yet important changes that can take place at the metalloprotein active sites when liquid-nitrogen-based cooling is used. The study also illustrates the need for direct measurement of the redox states of the metals, through X-ray absorption spectroscopy, simultaneously with the crystallographic measurements.

## 1. Introduction

X-ray-induced damage of metalloprotein active sites during crystallographic and X-ray absorption spectroscopic data collection can substantially affect the conclusions drawn from the structural data. An oxidized metal site may become partially or fully reduced, which can mask important differences that occur upon reduction or catalysis (Sommerhalter *et al.*, 2005; Champloy *et al.*, 2000; Penner-Hahn *et al.*, 1989; Chance *et al.*, 1980), or in some cases the damage may be sufficient to destroy the structure of the active site entirely (Yano *et al.*, 2005; Grabolle *et al.*, 2006). Although this radiolytic effect can sometimes be harnessed to create catalytic intermediates in a crystal that can then be structurally analyzed (Schlichting *et al.*, 2000; Berglund *et al.*, 2002), proper monitoring is required to be able to correlate a structure with a specific oxidation state (Berglund *et al.*, 2002). Where possible, a microspectrophotometer can be used to monitor changes in the visible absorption spectrum of the crystal during data collection, which can be then correlated with metal-site reduction (Karlsson *et al.*, 2000; Sjögren & Hajdu,

2001; Berglund *et al.*, 2002; Adam *et al.*, 2004; Chance *et al.*, 1980), but this technique is not generally used for studies of metalloproteins. The use of anomalous dispersion data for determination of oxidation state (Einsle *et al.*, 2007) could potentially be evolved to also monitor radiation damage. Traditionally, a crystal is not considered to be damaged by radiation until its diffracting power decreases by 50%. This measure of damage is not sensitive to the changes that rapidly occur at metal centers and other electron-affinic sites in as little as 90 s at 100 K at an intense X-ray source (Adam *et al.*, 2004).

Radiation damage occurs in stages (Kiefer, 1990; Henderson, 1990; Nave, 1995; O'Neill *et al.*, 2002). In the first stage, the X-ray photons interact with the atoms in the crystal, causing ionizations and electronic excitations through both absorption and scattering mechanisms. These effects are temperature-independent and depend on the energy of the X-rays and the amount of energy deposited per unit mass (dose). The deposition of energy can lead to sample heating and the breakage of bonds, as well as the formation of radical species, which then react with the protein components in the second stage of damage. The third stage of damage proceeds from the first two and involves the loss of lattice contacts and general destruction of crystalline order (Henderson, 1990; Teng & Moffat, 2000; Nave, 1995; O'Neill *et al.*, 2002). Reactive radicals are produced 'directly' from the ionization of the protein components or 'indirectly' from the excitation and ionization of the solvent water molecules (Symons, 1995). The excitation of water primarily leads to the formation of solvated electrons and hydroxyl radicals and, to a lesser extent, hydrogen radicals (von Sonntag & Schuchmann, 1994; Kiefer, 1990). These species, together with the electrons released from the protein atoms, are responsible for the secondary damage observed in proteins. This type of damage is considered to be temperature-dependent, with decreasing temperatures slowing the mobility of the radical species and increasing the rate of radical recombination (Kiefer, 1990; Henderson, 1990; Nave, 1995; O'Neill *et al.*, 2002). Early reports from pulsed radiolysis experiments have shown that electrons in proteins are mobile at 77 K and selectively move to electron sinks such as metal atoms and disulfide bonds, with the more electron-affinic metal sites being reduced first (Symons & Petersen, 1978; Ramakrishna Rao *et al.*, 1983; Jones *et al.*, 1987; Symons & Taiwo, 1992). Specific radiation-induced structural changes now have been observed by X-ray crystallography in disulfide bonds, the carboxyl groups of acidic residues, tyrosine residues and in chromophores such as retinal and flavin adenine dinucleotide (Weik *et al.*, 2000, 2002; Ravelli & McSweeney, 2000; Burmeister, 2000; Leiros *et al.*, 2001; Matsui *et al.*, 2002; Kort *et al.*, 2004).

While marked decreases in X-ray damage are observed upon moving from higher temperatures to ~100 K (Low *et al.*, 1966; Hope, 1988), the use of liquid He to reach even lower temperatures has not been regarded as necessary (Weik *et al.*, 2001; Teng & Moffat, 2002). Liquid He is considered to be useful for providing better crystal cooling, as a result of its increased thermal transport properties compared with liquid nitrogen (Garman, 1999), and for improving the rate of damage to the highest resolution data (Hanson *et al.*, 2002), but these advantages have not been considered to be sufficient for its universal adoption in macromolecular crystallography (Garman, 2003). It has recently been shown that the global damage to crystals of an iron-containing protein can be reduced during data collection by maintaining the crystals at 15 K instead of 90 K, whereas there is only a small change in the damage to a metal-free protein (Meents *et al.*, 2007). Still, more evidence is needed to support the conclusion that lowering the temperature beyond ~110 K can be extremely useful for preventing the specific secondary damage that affects metal sites, disulfide bonds and other susceptible groups before the use of liquid He will become standard practice during data collection from sensitive proteins.

Unlike a crystallographic experiment, an XAS experiment includes an *in situ* spectroscopic probe of X-ray damage or photoreduction. The EXAFS region provides geometric structural information about the metal active site, while the edge region reflects the electronic state of the metal atoms. Successive scans can be monitored to detect changes in either region. Unfortunately, it is not always straightforward to correlate structural results from EXAFS with those from crystallography because the resolutions of crystallographic experiments are usually lower than that of the EXAFS experiment and because there may be differences between the two structures analyzed, in addition to damage or reduction effects, that are a consequence of differences between the protein in solution and in a crystal (Dodd *et al.*, 2000). The recently developed instrumentation for single-crystal XAS at SSRL (Latimer *et al.*, 2005), which enables the XAS measurement of protein crystals under conditions similar to those of a typical crystallography experiment (Yano *et al.*, 2005; Corbett *et al.*, 2005), provides the perfect path for assessing the factors that influence X-ray damage of metalloproteins. Described herein is the use of the single-crystal instrumentation for the study of the impact of temperature on the dose-dependent photoreduction of the metalloprotein putidaredoxin (Pdx), a ~12 kDa $[Fe_2S_2]$-cluster-containing protein that is the specific reductant and effector of cytochrome P450 during camphor hydroxylation. Pdx was selected because it is representative of a large class of $[Fe_2S_2]$-cluster-containing proteins that function in electron transfer. Despite the importance of oxidation-state cycling in these proteins, a good structural description of the changes that occur in the $[Fe_2S_2]$ active site with reduction is lacking because in most of the structures reported the oxidation state of the protein was not given or proper consideration of photoreduction was not taken.

In this study, the X-ray absorption spectral changes in Pdx crystals measured at ~110 K and at ~40 K are compared with those in a Pdx solution at 7 K. A strong correlation between temperature and rate of photoreduction is observed, with a dramatic decrease in the rate and amount of damage found in the crystal measured at ~40 K compared with that measured at ~110 K. The structure of the $[Fe_2S_2]$ active site measured at ~110 K is found to be affected by this damage. These results

**Table 1**
Sample characteristics and experimental conditions.

| Sample | State | Crystal dimensions (μm) | *T* (K) | Maximum energy† (eV) | Scan time‡ (min) | No. of scans |
|---|---|---|---|---|---|---|
| Solution 1 | Oxidized | — | 7 | 8167 | 26.7 | 25§ |
| Solution 2 | Reduced | — | 7 | 8167 | ∼40 | 21 |
| Crystal 1 | Oxidized | 200 × 100 × 50 | ∼40 | 7771 | 22.2 | 6 |
| Crystal 2 | Reduced | 200 × 100 × 50 | ∼40 | 7987 | ∼32 | 19 |
| Crystal 3 | Oxidized | 100 × 100 × 50 | ∼110 | 7474 | 7.2 | 6 |
| Crystal 4 | Oxidized | 100 × 100 × 50 | ∼110 | 7591 | 14.3 | 8 |

† All scans started at 6785 eV. ‡ Scan time is the total exposure time per scan. The use of the mechanical shutter during data collection for the oxidized proteins limited the exposure time of these samples compared with the reduced samples. § Scans were collected from five different spots on two cells. No more than eight scans were collected per spot.

present unequivocal evidence that the use of liquid-helium-based cooling can substantially decrease the amount of damage to the active site of a metalloprotein during X-ray data collection. Furthermore, photoreduction is found to have a negative exponential, or logistic, dependence on dose at the temperatures studied here, which suggests that at sufficiently low temperatures, high doses and/or long data-collection times can be utilized without significant damage to the active sites of proteins such as Pdx.

## 2. Experimental

### 2.1. Sample preparation

A Cys73Ser/Cys85Ser variant of Pdx was recombinantly expressed in *Escherichia coli* and purified as described previously (Sevrioukova *et al.*, 2003). Solutions of Pdx for XAS analysis were 1.2 m*M* in protein (2.4 m*M* Fe) in 50 m*M* bis-Tris propane/acetate buffer pH 7.4 and 50% glycerol. Reduced samples additionally contained 10 m*M* sodium dithionite. All solution samples were loaded into 1 mm path-length 70 μl Lucite cells with Kapton tape windows, rapidly frozen and maintained at 77 K until data collection.

Crystals were grown using the hanging-drop vapor-diffusion method from droplets consisting of equal volumes (2–3 μl) of 14 mg ml$^{-1}$ Pdx in 100 m*M* bis-Tris propane/acetate buffer pH 7.4 and a reservoir solution consisting of 1.7 *M* ammonium sulfate, 50 m*M* sodium citrate pH 5.9 and 300 m*M* sodium potassium phosphate (Sevrioukova *et al.*, 2003). The crystals obtained under these conditions are flat plates belonging to space group $C222_1$, with unit-cell parameters $a = 50.2$, $b = 75.8$, $c = 107.7$ Å and two molecules of Pdx per asymmetric unit. Crystals were approximately 200 × 100 × 50 or 100 × 100 × 50 μm in size (see Table 1). As-isolated (oxidized) crystals were dipped in a solution of 30% saturated sodium malonate for cryoprotection. A reduced crystal was prepared in an anaerobic chamber by soaking an as-isolated crystal in a cryoprotectant solution containing 10 m*M* sodium dithionite until a color change from brown to pink was observed (Sevrioukova, 2005). The Pdx crystals were mounted on 24 mm CrystalCap Copper crystallography pins (Hampton), flash-frozen in liquid $N_2$ and maintained at 77 K until data collection.

### 2.2. XAS data collection

Solution X-ray absorption data were measured at SSRL (3 GeV, 70–100 mA beam conditions) using wiggler beamline 9-3 with an Si(220) double-crystal monochromator and two Rh-coated mirrors: a flat pre-monochromator mirror for harmonic rejection and vertical collimation and a toroidal post-monochromator mirror for focusing. The beam size was defined to be 1 × 4 mm by adjustable slits located after the monochromator. During data collection, the samples were maintained at 7 K inside an Oxford Instruments CF1208 liquid-helium continuous-flow cryostat. Data were collected as Fe $K\alpha$ fluorescence using a Canberra 30-element solid-state Ge-array detector. Radiation from elastic/inelastic scattering and Mn $K\alpha$ and Fe $K\beta$ fluorescence was minimized at the detector by placing a set of Soller slits with a Mn filter between the cryostat and the detector. The X-ray energy was calibrated to the inflection point at 7111.3 eV of a standard Fe foil measured concurrently with the samples. Photoreduction of the oxidized solution samples was limited by collecting no more than eight scans from any one spot on a frozen protein cell. Additionally, for the oxidized sample, a computer-controlled pneumatic shutter was automatically closed during monochromator movement to minimize the total sample-exposure time (Latimer *et al.*, 2005).

Single-crystal XAS data were also measured on SSRL beamline 9-3 using the single-crystal XAS instrumentation described by Latimer *et al.* (2005). The beam size was defined to be 0.5 × 0.5 mm. Scattered radiation was further limited by a set of JJ X-ray slits positioned directly in front of the crystal (Latimer *et al.*, 2005). The protein crystals were mounted on a Huber Kappa goniometer and maintained at either ∼40 K with a gaseous stream of liquid helium from a Cryo Industries liquid-helium cryostream (HFC-1645 LHE-Cryocool) or ∼110 K with a gaseous stream of liquid nitrogen from an Oxford Instruments liquid-nitrogen Cryojet. A flow rate of ∼0.5 l h$^{-1}$ was used in both cases. The crystals were aligned with their plate surfaces normal to the beam. XAS data were measured and calibrated as described above, with the exception that the Soller slit/filter assembly was not used. The experimental conditions used for the various crystal and solution samples are summarized in Table 1.

### 2.3. XAS data analysis

Normalized X-ray absorption-edge spectra between 6785 and 7470 eV were obtained using the program *XFIT* (Ellis & Freeman, 1995) to (i) generate a linear background absorption curve to fit the data in the pre-edge region, (ii) generate a two-segment polynomial spline to fit the EXAFS region and (iii) normalize the spectra to have an edge-jump of 1.0 between the background and spline curves at 7130 eV. Unlike previous photoreduction studies, there is no characteristic feature in the

edge of the reduced (or damaged) protein compared with the oxidized protein (Yano *et al.*, 2005; Penner-Hahn *et al.*, 1989) that can be used to monitor photoreduction. The difference spectrum between the oxidized and reduced solutions has a strong inflection point at 7117.1 eV (supplementary Fig. 1[1]). Therefore, the intensity at this point, calculated as an average over five data points, was monitored as a probe of photoreduction. The percentage error for this measurement, calculated by comparing the first scans from five spots of the oxidized solution, five scans from the reduced solution and five scans from the reduced crystal, is 1.3%.

EXAFS spectra were obtained by using the program *XFIT* to process the raw absorption data in the range 6780–7590 eV as above (Ellis & Freeman, 1995); however, the background curve was defined by a polynomial with weighted control points that fitted the data in the pre-edge region with a slope matching that of the post-edge region. Structural results were obtained by fitting the EXAFS spectra using the nonlinear least-squares fitting program *OPT* from the *EXAFSPAK* program suite (George, 1990). The *ab initio* theoretical phase and amplitude functions used in the fitting program were generated by *FEFF* (v.7.0; Mustre de Leon *et al.*, 1991; Rehr & Albers, 2000) from the coordinates of the $[Fe_2S_2]$ cluster in an oxidized Pdx crystal (PDB code 1oqq; Sevrioukova, 2005). During the fitting process, the variables for interatomic distance ($R$) and mean-square thermal and static deviation in $R$ ($\sigma^2$) were allowed to vary for all scattering components. The shift in the threshold energy ($\Delta E_0$) from 7130 eV was also varied for each fit, but constrained to be the same for all components. The amplitude-reduction factor ($S_0{}^2$) was fixed to a value of 1.0 for all fits.

### 2.4. Dose calculation

In order to measure the effects of X-ray photoreduction, the X-ray flux (in photons $s^{-1}$) at the sample and the absorbed X-ray dose must be calculated. The dose, $D$, which is typically expressed in Grays (Gy), where 1 Gy equals 1 J $kg^{-1}$, accounts for the number of photons hitting the sample as well as the proportion of photons that are absorbed per unit mass of sample (O'Neill *et al.*, 2002),

$$D = \frac{(\mu/\rho)nteE}{A} \times 10^{11}. \qquad (1)$$

The variables in the dose calculation (1) are the mass absorption coefficient $\mu/\rho$ ($cm^2\ g^{-1}$), which is element- and energy-dependent, the photon flux $n$ (photons $s^{-1}$), which is energy- and time-dependent, the irradiation duration $t$ (s), which is also energy-dependent in these experiments as the data scans are weighted so that more time is spent at higher energies where the signal-to-noise ratio in an EXAFS experiment is usually lower, the elementary charge $e$, which equals $1.6 \times 10^{-19}$ J $eV^{-1}$, the photon energy $E$ (eV) and the irradiation area $A$ ($\mu m^2$) (O'Neill *et al.*, 2002).

The photon flux on beamline 9-3 at 7100 eV/100 mA with a 0.5 × 0.5 mm beam size has been reported as ~$4 \times 10^{11}$ photons $s^{-1}$ (Latimer *et al.*, 2005). The photon flux is energy-dependent and also decays with time as the ring current decays. Thus, an energy- and time-dependent measure of photon flux would provide a more accurate calculation of dose than this approximation. The voltage produced in a nitrogen-filled open-flow gas ionization chamber located directly in front of the sample, which is routinely recorded as part of an XAS experiment, can provide this measure. The photon flux transmitted through the ion chamber, $I_T$, can be expressed in terms of the absorbed flux $I_A$, the linear absorption coefficient of the absorbing material $\mu$ ($cm^2\ g^{-1}$), the density of the material, $\rho$ (g $cm^{-3}$) and the chamber length $L$ (cm),

$$I_T = I_A[1/\exp(\mu\rho L) - 1]. \qquad (2)$$

Plots of $\exp(\mu\rho L)$ as a function of energy are available at http://www-cxro.lbl.gov (Henke *et al.*, 1993; Hubbell *et al.*, 1975; Gullikson, 2003). $I_T$ does not, however, represent the photon flux at the sample, as the beam must pass through the Kapton tape at the end of the ion chamber and air before it arrives at a crystal sample or Kapton tape, air and the cryostat windows before it arrives at a solution sample. These

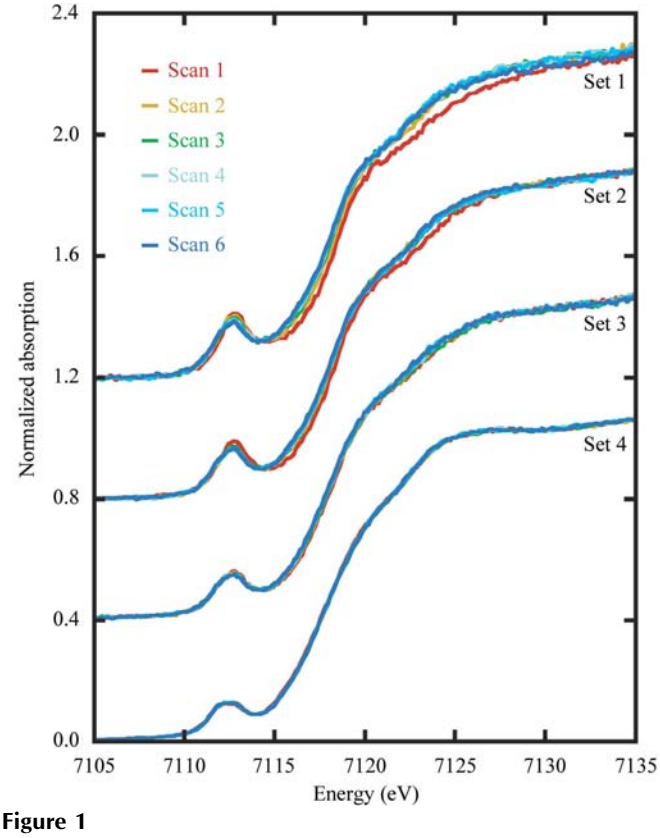


**Figure 1**
Offset normalized Fe *K* edge X-ray absorption spectra of Pdx in solutions and single crystals and at different temperatures. The spectra are, from top to bottom, oxidized crystal 3 at ~110 K (set 1), oxidized crystal 1 at ~40 K (set 2), oxidized solution 1 at 7 K (set 3) and reduced solution 2 at 7 K (set 4). Each set of spectra displays six consecutive scans. The time and dose per scan are not the same in each set. Note the reproducibility of the normalization across different scans for the reduced solution.

[1] Supplementary material has been deposited in the IUCr electronic archive (Reference: EA5070). Services for accessing this material are described at the back of the journal.

attenuations can be calculated using data available at http://www-cxro.lbl.gov (Henke *et al.*, 1993; Hubbell *et al.*, 1975; Gullikson, 2003). Additionally, because the crystals were smaller than the beam size, the fluxes for single-crystal measurements were scaled to represent only the portion of the beam that was incident on the crystal, assuming an experimentally established Gaussian intensity distribution of the beam within its defined limits. The final results for photon flux at the sample ($n$) reflect the sum of attenuated $I_T$ values over all energy points.

In addition to $n$, the calculation of dose requires $t$, $A$ and $\mu/\rho$. The time per energy point is recorded in an XAS data scan and can be summed to find $t$. The time between points, when the sample is not exposed to radiation, was neglected. Where the beam is smaller than the sample, as in the solution experiments, $A$ is defined by the beam size ($5.66 \times 10^6$ µm$^2$ for a cell positioned 45° relative to a 1 × 4 mm beam); for the crystals, which were smaller than the beam, $A$ is defined by the crystal size (see Table 1). The determination of $\mu/\rho$ requires the calculation of the mass fractions of all the elements in each sample. Because of the relatively small amounts of protein and buffer in the solution, the solution density was assumed to be that of a 50:50 mixture of glycerol in water. Mass fractions in the solution were calculated based on the reported concentrations of protein and buffer. The solution was found to comprise 9.8% H, 22.2% C, 0.2% N, 67.8% O, 0.02% S and 0.01% Fe. The *XCOM* tool (Berger *et al.*, 2005) was used to calculate $\mu/\rho$ as a function of $E$ for this mixture of elements. The Matthews coefficient, $V_M$, of the Pdx crystals studied here is 2.25 Å$^3$ Da$^{-1}$, which corresponds to a solvent content of 45.3% (Matthews, 1968). Pdx crystals with this solvent content have mass compositions of 8% H, 10.6% C, 30.4% N, 46.9% O, 0.3% Na, 0.2% K, 0.2% P, 2.4% S and 0.6% Fe. Although the percentage of Fe is low in the crystals, it increases $\mu/\rho$ by ∼13% above the Fe edge at 7112.3 eV. Therefore, two different $\mu/\rho$ curves were used in the dose calculation, one below and one above 7112.3 eV.[2]

Using $n$, $t$, $A$ and $\mu/\rho$ as defined above, dose was calculated according to (1) for each energy point in a scan and then summed over all energies and all scans. Dose for a single scan was considered to be the dose absorbed up to an energy of 7117.1 eV for edge analysis or to the scan end for EXAFS analysis.

## 3. Results

### 3.1. Quantification of photoreduction

Samples of Pdx were measured in solution at 7 K and in single crystals at ∼40 K (crystals 1 and 2) and at ∼110 K (crystals 3 and 4) (see Table 1). The X-ray absorption-edge spectra of the oxidized Pdx samples, especially those of the crystal measured at ∼110 K (crystal 3), changed over time as successive data scans were collected (Fig. 1). In contrast, the spectra of the reduced Pdx samples did not change during the course of data collection (Fig. 1). The changes observed in the oxidized-sample spectra (shifts in the edge position to lower energy, decreases in edge intensity at 7123.6 eV and decreases in pre-edge intensity to ∼7113 eV) are consistent with the changes observed upon reduction of the oxidized [$Fe^{III}_2S_2$] metal centers in this protein and are attributed to photoreduction of the oxidized proteins by the X-ray beam. The samples were measured over different amounts of time and were exposed to different X-ray doses; thus, the scan comparison shown in Fig. 1 is not an accurate basis for evaluating the changes that occurred. Therefore, the edge change as a function of dose was quantitatively monitored in order to provide a greater insight into the photoreduction of Pdx.

The average normalized X-ray absorption-edge intensity at 7117.1 eV was selected as a sensitive marker of the change in the edge with photoreduction. For the reduced solution (solution 2) and reduced crystal (crystal 2), the intensity at this position is constant within 1.3% error. However, the intensity at this position cannot be used as an absolute marker of photoreduction across the different samples because the crystal spectra have different shapes than the solution spectra (Fig. 2). It was expected that the spectra of the first scans from the oxidized crystals would appear to be more reduced than that from the oxidized solution, as these samples appeared to photoreduce faster than the solution sample. However, the opposite effect was observed: the first scan edges in the crystal spectra are shifted to higher energy relative to the solution first scan edge spectrum and the pre-edges in these spectra are more intense (Fig. 2). Although it may be that the rigid environment in the crystal enforces a less centrosymmetric environment around the Fe centers that leads to an enhanced

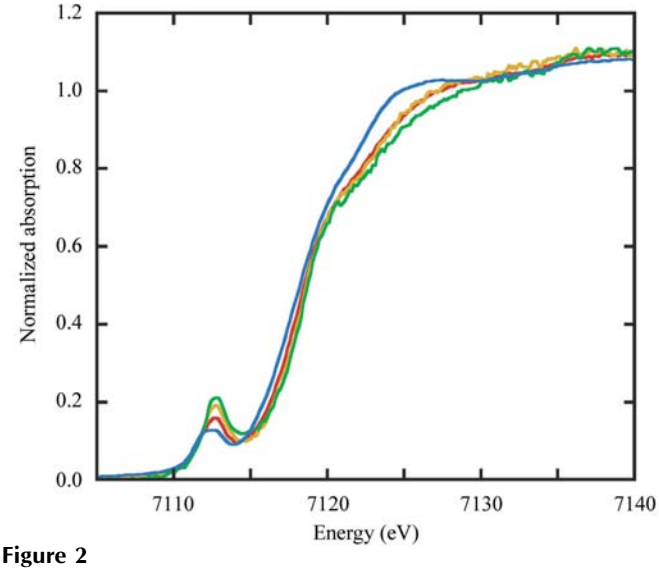


**Figure 2**
Normalized Fe *K* edge X-ray absorption spectra of Pdx in solutions and single crystals. The spectra are the average of the five first scans (one from each of the five spots irradiated) from oxidized Pdx solution 1 (red) and reduced Pdx solution 2 (blue) and the first scan from oxidized Pdx crystal 1 (yellow) and from oxidized Pdx crystal 3 (green). The crystal spectra are distorted by self-absorption in the thin but concentrated protein crystals.

[2] $\mu/\rho$ accounts for the total absorbed energy, but does not account for the energy that is subsequently lost owing to fluorescence (Murray *et al.*, 2005). This discrepancy will artificially increase the dose estimates, having an impact on the crystal measurements slightly more than the solution measurements.

pre-edge intensity in a crystal compared with a solution, this effect would be constant across the various crystals measured, which was not the case. Instead, the distortions observed in the crystal spectra are consistent with self-absorption in the thin but concentrated crystal samples (Jaklevic *et al.*, 1977; Lytle, 1988; Meitzner & Fischer, 2002). This effect is more pronounced in the edge than the pre-edge, leading to a higher pre-edge-to-edge ratio in a normalized distorted spectrum compared with a regular spectrum (Meitzner & Fischer, 2002). The difference in edge intensity in the crystals could also be related to a polarization effect; however, the edge spectra of a Pdx crystal similar to those studied here was constant across several different crystal orientations (data not shown).

The relative changes in the edge position at 7117.1 eV would not be affected by self-absorption and therefore can be used to compare between the different samples. As shown in Fig. 3, Pdx intensity at 7117.1 eV exhibits logistic growth with increasing dose: there is a large change upon initial exposure and the rate of change then slows with increasing dose. This behavior is most easily observed in crystal 3 (Fig. 3*c*), which exhibits the steepest growth curve. In the solution sample (Fig. 3*a*) and to a lesser extent in crystal 1 (Fig. 3*b*) the changes are small and are more affected by experimental error than in crystal 3. The exponential fits to the data in Fig. 3 can be used to calculate the theoretical edge intensity at zero dose. When the percentage change in intensity from this calculated zero-dose value is plotted for all samples on the same dose scale (Fig. 4*a*), it is clear that the samples measured at 7 and ∼40 K are similarly affected by dose, whereas that measured at ∼110 K changes much more rapidly with dose. It is not possible to make a one-to-one comparison between Pdx in solution and in single crystals, because the protein is in a different environment in solution than in the crystal and this may have an impact on the rate of photoreduction (Yano *et al.*, 2005). Therefore, reducing the temperature below ∼110 K is shown here to decrease the rate of photoreduction in a Pdx crystal, but it is not possible to determine from these data whether reducing the temperature below ∼40 K would have any further impact.

It is possible to calculate the theoretical percentage of photoreduction in the samples based on the change in intensity from the zero-dose value by assuming that the edge intensity of a fully reduced sample represents 100% reduction. Using this measure, the oxidized solution is considered to be ∼50% reduced after a dose of $\sim 2 \times 10^6$ Gy, whereas the oxidized crystal measured at ∼110 K (crystal 3) is ∼150% reduced after receiving half that dose. A reduction of over 100% suggests that the Fe site has been reduced beyond the mixed-valence state to an all-ferrous state. The radiolytic reduction of both $[Fe_2S_2]$- and $[Fe_4S_4]$-cluster-containing protein solutions to the all-ferrous state by exposure to a white beam for 100 min at 77 K has been reported previously (Yoo, Meyer *et al.*, 1999; Yoo, Angove *et al.*, 1999). In the case of the $[Fe_2S_2]$ protein, the resulting solution was shown by Mössbauer spectroscopy to contain 50% of the $[Fe^{II}{}_2S_2]$ cluster (Yoo, Meyer *et al.*, 1999), which is equivalent to the observed ∼150% reduction from the oxidized $[Fe^{III}{}_2S_2]$ state in crystal 3 (Fig. 4*b*). However, there is a high level of uncertainty in the photoreduction values reported here because it is not clear that a photoreduced sample representing an $[Fe^{III}Fe^{II}S_2]$ state would have the same X-ray absorption-edge shape as a chemically reduced sample. Furthermore, the reduced crystal (crystal 2) does not have exactly the same edge and EXAFS features as the reduced solution (solution 2), which suggests that chemical reduction of the protein in the crystal may not be complete or may be constrained so that a slightly different reduced state is achieved than that which occurs in solution.

### 3.2. Structural studies

EXAFS analyses of Pdx proteins at different levels of reduction can provide a metric for the structural changes that accompany photoreduction. Three types of scattering interactions can be detected by the EXAFS experiment: Fe–S

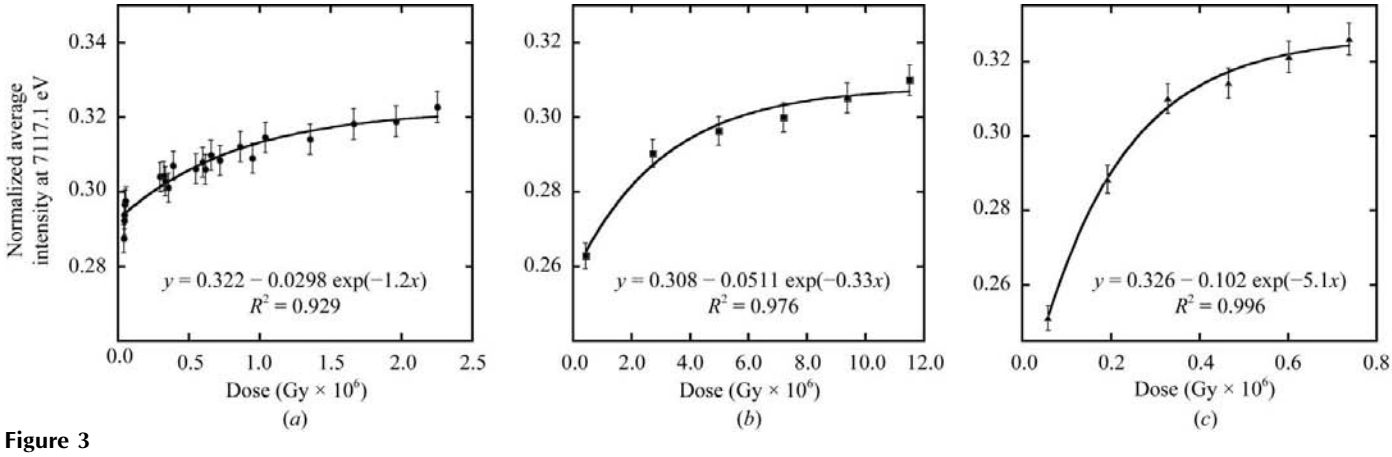


**Figure 3**
Plots of edge intensity at 7117.1 eV *versus* dose for oxidized Pdx at 7 K in solution 1 (*a*), at ∼40 K in crystal 1 (*b*) and at ∼110 K in crystal 3 (*c*). Solution 1 in (*a*) includes five sets of points from five spots on two separately measured solution cells. Normalized average intensity at 7117.1 eV was calculated by averaging the intensity at five data points centered at 7117.1 eV in the normalized X-ray absorption spectra shown in Fig. 1. The data were fitted to exponential curves; linear or quadratic curves do not accurately reproduce the shape of the data. The *x* and *y* scales of the plots were chosen to best highlight the data and are not the same in all panels; however, the magnitudes of the *y* scales are equivalent.

scattering from the first-shell S atoms in the inorganic cluster and Cys ligands, Fe–Fe scattering across the cluster and long-range Fe–S scattering from the Cys residues on opposite sides of the cluster (see Fig. 5). This last interaction provides a probe of how the residues in the $[Fe_2S_2]$-cluster active site respond to the change in cluster oxidation state. Because of the rapid rate of Pdx photoreduction at ~110 K, the EXAFS and X-ray absorption edge data were measured from different crystals and EXAFS were only collected to a $k$ of 11 Å$^{-1}$. Over this data range, the oxidized solution, which is at most 35% photoreduced on average, is fitted with four S scatterers at 2.25 Å, one Fe scatterer at 2.67 Å and two S scatterers at 4.44 Å (Table 2). After chemical reduction, as in solution 2, the distances for all of these scattering interactions are increased by at least 0.03 Å and the disorder in the long-range Fe–S scattering is substantially increased (Table 2).

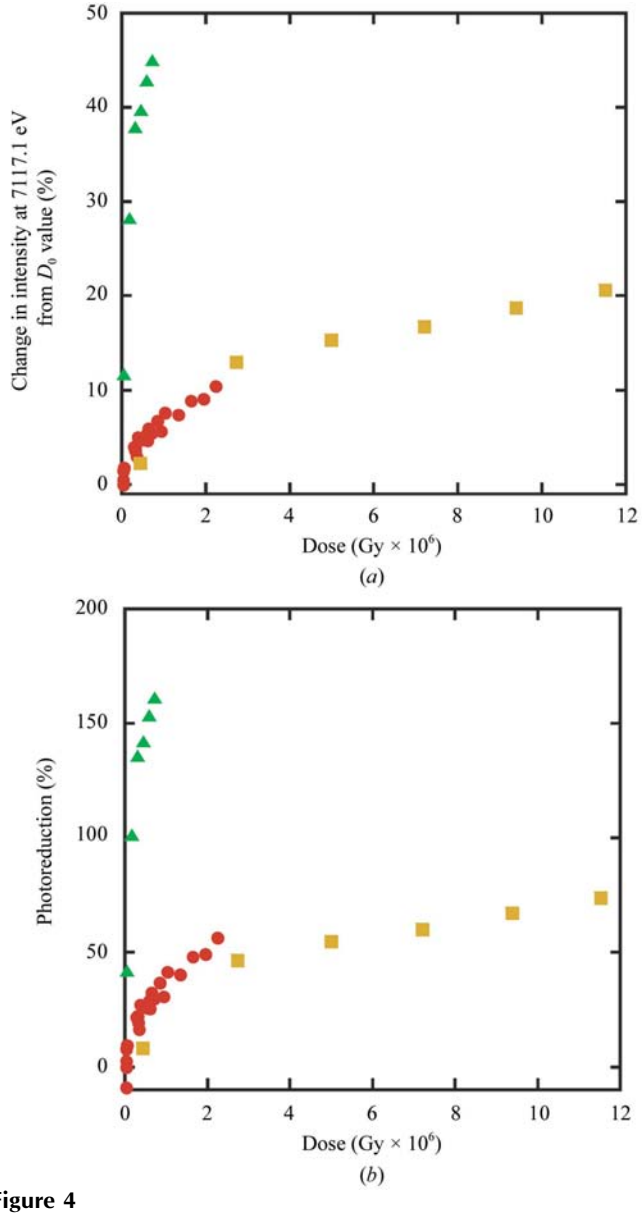


**Figure 4**
Changes in Fe $K$ edge X-ray absorption spectra with increasing dose for oxidized Pdx at 7 K in solution 1 (red circles), at ~40 K in crystal 1 (yellow squares) and at ~110 K in crystal 3 (green triangles). (*a*) Percentage change in the normalized average intensity at 7117.1 eV from the theoretical zero-dose value calculated from the curve-fitting equations in Fig. 3. (*b*) Percentage photoreduction, where photoreduction is calculated by scaling the percentage change in (*a*) so that a change of 100% is equal to the percentage difference between the zero-dose intensity value and the fully reduced value for that sample (solution 2 is the reduced equivalent of solution 1 and crystal 2 is the reduced equivalent of crystal 1). A fully reduced sample equivalent to crystal 3 was not available, so the crystal 2 value was used.

Crystal 2, which was chemically reduced and measured at ~40 K, is fitted with scattering distances analogous to those found for the reduced solution (Table 2). The data set from crystal 1, which was similarly measured at ~40 K, represents an average state that is at most 61% reduced. The fitting results for this data set are consistent with those obtained for the oxidized solution (Table 2); however, the EXAFS Fourier transform shows reduced intensity in the second peak compared with the other samples (Fig. 6). This change in peak height is not a result of photoreduction, as the peak height was not observed to change over time and that of crystal 4, which was substantially photoreduced, is unchanged. Rather, the decrease in peak height is probably a polarization effect owing to the orientation of the crystal in the X-ray beam. If the Fe–Fe scattering vector were strictly 90° from the beam polarization vector, no Fe–Fe scattering would be observed; if it were collinear with the polarization vector, then the Fe–Fe scattering would be enhanced threefold. In this case, the EXAFS data are well fitted with a coordination number of 0.5, which would correspond to an angle between the Fe–Fe scattering vector and the polarization vector of ~65°. The crystallographic coordinates from a Pdx crystal similar to those measured here (PDB code 1oqq; Sevrioukova, 2005) indicate that there is one orientation, along the $c$ axis, in which all of the $[Fe_2S_2]$ clusters would be arranged approximately normal to the polarization vector. Thus, it is possible that the crystal could have been orientated with the average Fe–Fe scattering vector tilted away from the polarization vector. Unfortunately, it was not possible to collect a diffraction pattern from this crystal, so the exact orientation cannot be verified.

The EXAFS data from the oxidized crystal measured at ~110 K were found to represent an average state that is at most 150% reduced. Because the structural changes between the oxidized and reduced states of Pdx are small, there are not many obvious differences between the EXAFS of oxidized and reduced samples. One feature that does stand out is the position of the fourth peak in the EXAFS spectrum at

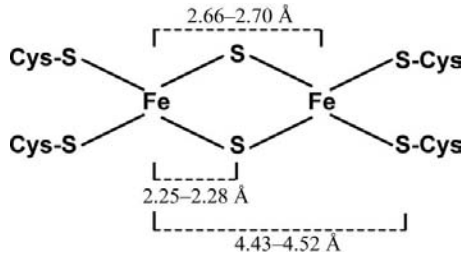


**Figure 5**
Diagram of the Pdx $[Fe_2S_2]$ center.

**Table 2**
EXAFS fit results.

All fits were calculated over a $k$ range of 2–11 Å$^{-1}$. Errors are estimated to be 25% for coordination numbers ($N$) and 0.01–0.02 Å for distances ($R$).

| | | | Scatterer | | | | | | |
|---|---|---|---|---|---|---|---|---|---|
| | | | 4 S | | 1 Fe | | 2 S | | |
| Sample | Dose (Gy × 10$^6$) | Percentage reduced | $R$ (Å) | $\sigma^2$ (Å$^2$) | $R$ (Å) | $\sigma^2$ (Å$^2$) | $R$ (Å) | $\sigma^2$ (Å$^2$) | $F$† |
| Solution 1 | 7.2 | ∼35‡ | 2.25 | 0.0076 | 2.67 | 0.0055 | 4.44 | 0.0073 | 0.16 |
| Solution 2 | 6.6 | 100 | 2.28 | 0.0064 | 2.70 | 0.0079 | 4.52 | 0.0123 | 0.17 |
| Crystal 1 | 13.2 | ∼61‡ | 2.25 | 0.0082 | 2.66§ | 0.0061§ | 4.43 | 0.0092 | 0.19 |
| Crystal 2 | 48.8 | 100 | 2.28 | 0.0077 | 2.70 | 0.0058 | 4.50 | 0.0076 | 0.20 |
| Crystal 4 | 1.6 | ∼150‡ | 2.26 | 0.0082 | 2.69 | 0.0066 | 4.52 | 0.0102 | 0.27 |

† The fit error ($F$) is defined as $F = [\sum k^6(\chi_{\rm exptl} - \chi_{\rm calcd})^2 / \sum k^6 \chi^2_{\rm exptl}]^{1/2}$. ‡ Values were determined by calculating the theoretical edge intensity and corresponding percentage photoreduction for each scan based on the cumulative dose at the end of the scan using the equations in Fig. 3. The total photoreduction value is the average photoreduction value for all scans in the data set. Because of the error in using calculated values, this estimate most likely represents an upper level for the possible amount of photoreduction. § A coordination number of 0.5 instead of 1 was used for this scatterer.

visual appearance of the EXAFS data and the fitting results support the conclusion that photoreduction alters the structure of the active site in this protein, but that the effect is not identical to reduction with a chemical reductant such as sodium dithionite.

One reported crystal structure of oxidized Cys73Ser/Cys85Ser Pdx at 1.47 Å resolution indicates that the structure was determined at 110 K on SSRL beamline 7-1 at 1.08 Å (11.5 keV) over a span of 197 min (Sevrioukova *et al.*, 2003). These parameters correspond to a total dose of ∼3.5 × 10$^5$ Gy, which, for a crystal comparable to crystal 1, would correspond to a total amount of photoreduction of ∼140% by the end of data collection, or 70% reduction on average, which is similar to the amount of photoreduction in crystal 1. In this case, as in crystal 1, the average [$Fe_2S_2$] distances are mostly consistent with an oxidized site: Fe—S at 2.25 ± 0.05 Å, Fe···Fe at 2.72 ± 0.01 Å and Fe···S(Cys) at 4.47 ± 0.04 Å. The average Fe···Fe distance is longer than those found by EXAFS, but 0.02 Å shorter than the Fe···Fe distance in the structure of a reduced Pdx crystal determined at a similar resolution (Sevrioukova, 2005) and therefore consistent with the trend of an increase in the Fe···Fe distance with reduction. Of all the structural parameters, the long-range Fe···S(Cys) distance may show the effects of photoreduction. When diffraction data for an oxidized Pdx crystal were measured at a lower flux source, the average short-range Fe—S and Fe···Fe distances in the 2.00 Å resolution structure were the same as those measured at SSRL, but the average Fe···S(Cys) distance was 4.42 ± 0.06 Å (Sevrioukova *et al.*,

∼9.5 Å$^{-1}$: it is clearly shifted to lower $k$ in the two fully reduced samples (solution 2 and crystal 2) compared with the ∼35% and ∼61% photoreduced samples (solution 1 and crystal 1) (Fig. 6). The position of the fourth EXAFS peak of the ∼150% photoreduced sample is more consistent with the position of the reduced samples than the oxidized samples (Fig. 6). The EXAFS data from this sample are fitted with four S scatterers at 2.26 Å, one Fe scatterer at 2.69 Å and two long-range Fe–S scatterers at 4.52 Å. These results present a mixed picture of the changes that take place with photoreduction. The long-range Fe–S scattering is clearly consistent with a reduced sample, whereas the distance of the short-range Fe–S scattering is not significantly increased relative to the more oxidized samples. The Fe–Fe scattering distance is increased and is consistent with a reduced sample, although it is also within experimental error of the oxidized-solution value. The

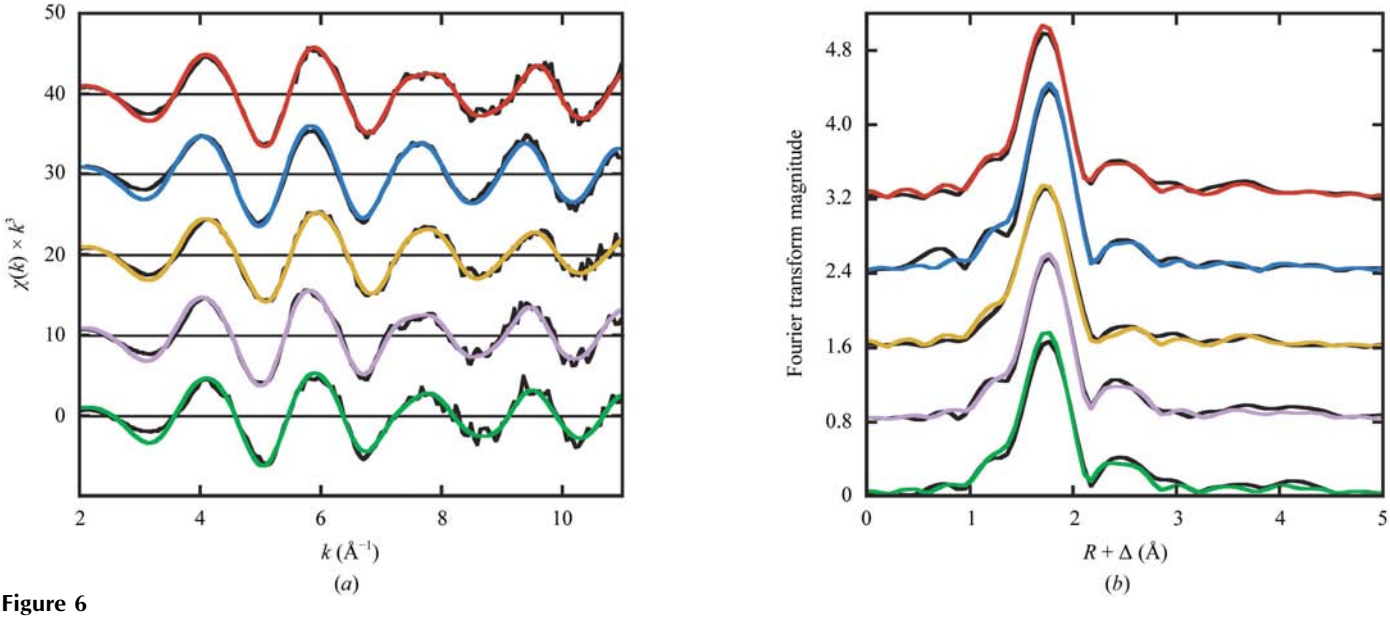


**Figure 6**
Pdx EXAFS data and fits from Table 2. (*a*) Offset EXAFS data (black) and fits for Pdx in solution 1 (red), solution 2 (blue), crystal 1 (yellow), crystal 2 (violet) and crystal 4 (green). (*b*) Offset Fourier transforms of the spectra in (*a*).

2003), which is more consistent with the results obtained from XAS for an oxidized site. An oxidized C73S Pdx mutant measured under the same conditions at SSRL as the Cys73Ser/Cys85Ser mutant described above appeared from its $[Fe_2S_2]$ distances to be reduced, having average Fe···Fe and Fe—S distances that were longer than its chemically reduced counterpart, the structure of which was determined at the slightly lower resolution of 1.84 Å compared with 1.65 Å (Sevrioukova *et al.*, 2003; Sevrioukova, 2005). It may be that this type of Pdx crystal is more sensitive to radiation damage than the other. In the only other study of an $[Fe_2S_2]$ protein in both oxidized and reduced states, both structures were of moderately high resolution, 1.30 and 1.17 Å, respectively, and the average Fe—S, Fe···Fe and Fe···S(Cys) distances were found to be the same in the two states and to be consistent with the reduced form of the cluster (Morales *et al.*, 1999). The comparison of these crystallographic results with the single-crystal EXAFS results reported here exposes two significant problems with structural data obtained from crystallography at 110 K: (i) photoreduction-induced structural change can and does occur during data collection and (ii) the precision of the crystallographic experiment, which is of the order of 0.04–0.07 Å for structures in the 1.3–2.0 Å resolution range (Guss *et al.*, 1992), may not be sufficient to detect the subtle differences that exist between oxidized, photoreduced and chemically reduced forms of an enzyme. The first problem can be resolved to a large extent by collecting data at a lower temperature. At 40 K, the beamline 7-1 dose of $\sim 3.5 \times 10^5$ Gy would correspond to only 10% photoreduction of Pdx overall, allowing the structure to be confidently assigned to an oxidized state.

## 4. Conclusion

Through the study by XAS of Pdx in single crystals at ∼110 and ∼40 K and in solutions at 7 K, it is shown that photoreduction of an $[Fe^{III}{}_2S_2]$ active site increases logistically with dose and that there is an approximately 30-fold decrease in the rate of dose-dependent photoreduction between ∼110 and ∼40 K. The dose required to reduce Pdx at ∼110 K by as much as 150% was $\sim 1 \times 10^6$ Gy, far less than the maximum theoretical dose for crystal damage of $3 \times 10^7$ Gy (Owen *et al.*, 2006). At ∼40 K, however, a dose of $\sim 1 \times 10^7$ Gy, although damaging, did not significantly perturb the structure of the active site. These results indicate that lower temperatures can substantially decrease the amount of damage to a metalloprotein crystal and allow much higher X-ray doses/data-collection times before damage to the metal active site becomes significant. The damage could theoretically be reduced even further by keeping the absorption coefficient of the crystal low and thereby reducing the dose, perhaps by changing the composition of the solvent in the crystal. Because electron-transfer rates and probabilities can vary with protein structure and the oxidation potential of the active site, the temperature-dependence and rate of photoreduction may be different in different systems (Gray & Winkler, 2003; Beratan *et al.*, 2005). In most cases, however, a temperature dependence, such as that observed here, would be expected because the electrons generated by X-ray radiolysis are randomly distributed with respect to a metal site and therefore only a small subset would likely be optimized for an athermal reaction.

Interestingly, despite an edge change in the oxidized crystal measured at ∼40 K that indicated as much as 61% photoreduction overall, the EXAFS-derived structure of the $[Fe_2S_2]$ active site was found to be consistent with an oxidized cluster. It may be that these results indicate that the structural change does not proceed immediately from the electronic change. There is uncertainty in the photoreduction calculation, however, so it may rather be that the crystal was not as reduced as it appeared to be from the edge change, although it was clearly partially reduced. Both edge and EXAFS changes were apparent in the crystal measured at ∼110 K. In addition to a dramatic edge shift in this crystal consistent with photoreduction beyond the reduced state obtainable with sodium dithionite, the EXAFS-derived Fe···Fe distance and Fe···S(Cys) distances increased to distances similar to those found in chemically reduced Pdx samples. Thus, the magnitude of photoreduction in the crystal at ∼110 K is sufficient to cause structural changes at the protein active site. These results have important implications for crystallography of metalloproteins and, specifically, $[Fe_2S_2]$-cluster-containing proteins, where photoreduction has hindered the development of a complete description of the structural changes that accompany oxidation-state cycling. For instance, the change in the long-range Fe···S(Cys) distance of almost 0.1 Å upon reduction, which was apparent in the XAS study but masked in the crystallographic study, may be related to rearrangements in the Pdx active site that signal downstream conformational changes in its redox partner, P450, as part of the electron-transfer reaction.

This study and others have shown the utility of using single-crystal XAS to correlate the oxidation state and high-precision metrical details of a metal active site with crystallographic results from the protein as a whole (Yano *et al.*, 2005, 2006). These studies also clearly recommend the standard use of liquid-helium-based cooling for metalloprotein crystallography to limit the damage or photoreduction of radiation-sensitive sites and illustrate the importance of monitoring radiation damage through a complementary *in situ* method such as XAS.

We acknowledge the contribution of A. L. Tenderholt for his helpful discussions regarding data normalization and processing. This work was supported by NIH grants RR-001209 (KOH), GM-33688 (TLP) and GM-67367 (IFS). XAS data were measured at SSRL, which is supported by the DOE, Office of Basic Energy Sciences. The SSRL Structural Molecular Biology Program is supported by the NIH, National Center for Research Resources, Biomedical Technology Program and by the DOE, Office of Biological and Environmental Research. The project described was supported by Grant No. P41 RR-001209 from the National Center for

Research Resources (NCRR), a component of the National Institutes of Health (NIH), and its contents are solely the responsibility of the authors and do not necessarily represent the official view of NCRR or NIH.

## References


Adam, V., Royant, A., Nivière, V., Molina-Heredia, F. P. & Bourgeois, D. (2004). *Structure*, **12**, 1729–1740.

Beratan, D. N., Betts, J. N. & Onuchic, J. N. (2005). *Science*, **252**, 1285–1288.

Berger, M. J., Hubbell, J. H., Seltzer, S. M., Chang, J., Coursey, J. S., Sukumar, R. & Zucker, D. S. (2005). *XCOM: Photon Cross Sections Database.* http://physics.nist.gov/PhysRefData/Xcom/Text/XCOM.html.

Berglund, G. I., Carlsson, G. H., Smith, A. T., Szöke, H., Henricksen, A. & Hajdu, J. (2002). *Nature (London)*, **417**, 463–468.

Burmeister, W. P. (2000). *Acta Cryst.* D**56**, 328–341.

Champloy, F., Gruber, K., Jogl, G. & Kratky, C. (2000). *J. Synchrotron Rad.* **7**, 267–273.

Chance, B., Angiolillo, P., Yang, E. K. & Powers, L. (1980). *FEBS Lett.* **112**, 178–182.

Corbett, M. C., Tezcan, F. A., Einsle, O., Walton, M. Y., Rees, D. C., Latimer, M. J., Hedman, B. & Hodgson, K. O. (2005). *J. Synchrotron Rad.* **12**, 28–34.

Dodd, F. E., Abraham, Z. H. L., Eady, R. R. & Hasnain, S. S. (2000). *Acta Cryst.* D**56**, 690–696.

Einsle, O., Andrade, S. A., Dobbek, H., Meyer, J. & Rees, D. C. (2007). *J. Am. Chem. Soc.* **129**, 2210–2211.

Ellis, P. J. & Freeman, H. C. (1995). *J. Synchrotron Rad.* **2**, 190–195.

Garman, E. (1999). *Acta Cryst.* D**55**, 1641–1653.

Garman, E. (2003). *Curr. Opin. Struct. Biol.* **13**, 545–551.

George, G. N. (1990). *EXAFSPAK.* Stanford Synchrotron Radiation Laboratory, Stanford, CA, USA.

Grabolle, M., Haumann, M., Müller, C., Liebisch, P. & Dau, H. (2006). *J. Biol. Chem.* **281**, 4580–4588.

Gray, H. B. & Winkler, J. R. (2003). *Q. Rev. Biophys.* **36**, 341–372.

Gullikson, E. M. (2003). *X-ray Interaction with Matter Calculator.* http://www-cxro.lbl.gov/optical_constants/.

Guss, J. M., Bartunik, H. D. & Freeman, H. C. (1992). *Acta Cryst.* B**48**, 790–811.

Hanson, B. L., Harp, J. M., Kirschbaum, K., Schall, C. A., DeWitt, K., Howard, A., Pinkerton, A. A. & Bunick, G. J. (2002). *J. Synchrotron Rad.* **9**, 375–381.

Henderson, R. (1990). *Proc. Natl Acad. Sci. USA*, **241**, 6–8.

Henke, B. L., Gullikson, E. M. & Davis, J. C. (1993). *At. Data Nucl. Data Tables*, **54**, 181–342.

Hope, H. (1988). *Acta Cryst.* B**44**, 22–26.

Hubbell, J. H., Veigele, W. J., Briggs, E. A., Brown, R. T., Cromer, D. T. & Howerton, R. J. (1975). *J. Phys. Chem. Ref. Data*, **4**, 471–538.

Jaklevic, J., Kirby, J. A., Klein, M. P. & Robertson, A. S. (1977). *Solid State Commun.* **23**, 679–682.

Jones, G. D. D., Lea, J. S., Symons, M. C. R. & Taiwo, F. A. (1987). *Nature (London)*, **330**, 772–773.

Karlsson, A., Parales, J. V., Parales, R. E., Gibson, D. T., Eklund, H. & Ramaswamy, S. (2000). *J. Inorg. Biochem.* **78**, 83–87.

Kiefer, J. (1990). *Biological Radiation Effects.* Berlin: Springer-Verlag.

Kort, R., Komori, H., Adachi, S., Miki, K. & Eker, A. (2004). *Acta Cryst.* D**60**, 1205–1213.

Latimer, M. J., Ito, K., McPhillips, S. E. & Hedman, B. (2005). *J. Synchrotron Rad.* **12**, 23–27.

Leiros, H.-K. S., McSweeney, S. M. & Smalås, A. O. (2001). *Acta Cryst.* D**57**, 488–497.

Low, B. W., Chen, C. C. H., Berger, J. E., Singman, L. & Pletcher, J. F. (1966). *Proc. Natl Acad. Sci. USA*, **56**, 1746–1750.

Lytle, F. W. (1988). *Applications of Synchrotron Radiation*, edited by H. Winick, D. Xian, M.-H. Ye & T. Huang, pp. 135–224. New York: Gordon & Breach.

Matsui, Y., Sakai, K., Murakami, M., Shiro, Y., Adachi, S., Okumura, H. & Kouyama, T. (2002). *J. Mol. Biol.* **324**, 469–481.

Matthews, B. W. (1968). *J. Mol. Biol.* **33**, 491–497.

Meents, A., Wagner, A., Schneider, R., Pradervand, C., Pohl, E. & Schulze-Briese, C. (2007). *Acta Cryst.* D**63**, 302–309.

Meitzner, G. D. & Fischer, D. A. (2002). *Microchem. J.* **71**, 281–286.

Morales, R., Chron, M.-H., Hudry-Clergeon, G., Pétillot, Y., Norager, S., Medina, M. & Frey, M. (1999). *Biochemistry*, **38**, 15764–15773.

Murray, J. W., Rudiño-Piñera, E., Owen, R. L., Grininger, M., Ravelli, R. B. G. & Garman, E. F. (2005). *J. Synchrotron Rad.* **12**, 268–275.

Mustre de Leon, J., Rehr, J. J. & Zabinsky, S. I. (1991). *Phys. Rev. B*, **44**, 4146–4156.

Nave, C. (1995). *Radiat. Phys. Chem.* **45**, 483–490.

O'Neill, P., Stevens, D. L. & Garman, E. F. (2002). *J. Synchrotron Rad.* **9**, 329–332.

Owen, R. L., Rudiño-Piñera, E. & Garman, E. F. (2006). *Proc. Natl Acad. Sci. USA*, **103**, 4912–4917.

Penner-Hahn, J. E., Murata, M., Hodgson, K. O. & Freeman, H. C. (1989). *Inorg. Chem.* **28**, 1826–1832.

Ramakrishna Rao, D. N., Symons, M. C. R. & Stephenson, J. M. (1983). *J. Chem. Soc. Perkin Trans. 2*, pp. 727–730.

Ravelli, R. B. G. & McSweeney, S. (2000). *Structure*, **8**, 315–328.

Rehr, J. J. & Albers, R. C. (2000). *Rev. Mod. Phys.* **72**, 621–654.

Schlichting, I., Berendzen, J., Chu, K., Stock, A. M., Maves, S. A., Benson, D. E., Sweet, R. M., Ringe, D., Petsko, G. A. & Sligar, S. G. (2000). *Science*, **287**, 1615–1622.

Sevrioukova, I. F. (2005). *J. Mol. Biol.* **347**, 607–621.

Sevrioukova, I. F., Garcia, C., Li, H., Bhaskar, B. & Poulos, T. L. (2003). *J. Mol. Biol.* **333**, 377–392.

Sjögren, T. & Hajdu, J. (2001). *J. Biol. Chem.* **276**, 13072–13076.

Sommerhalter, M., Lieberman, R. L. & Rosenzweig, A. C. (2005). *Inorg. Chem.* **44**, 770–778.

Sonntag, C. von & Schuchmann, H.-P. (1994). *Methods Enzymol.* **233**, 3–20.

Symons, M. C. R. (1995). *Radiat. Phys. Chem.* **45**, 837–845.

Symons, M. C. R. & Petersen, R. L. (1978). *Proc. R. Soc. London Ser. B*, **201**, 285–300.

Symons, M. C. R. & Taiwo, F. A. (1992). *J. Chem. Soc. Perkin Trans. 2*, pp. 1413–1415.

Teng, T. & Moffat, K. (2000). *J. Synchrotron Rad.* **7**, 313–317.

Teng, T.-Y. & Moffat, K. (2002). *J. Synchrotron Rad.* **9**, 198–201.

Weik, M., Bergès, J., Raves, M. L., Gros, P., McSweeney, S., Silman, I., Sussman, J. L., Houée-Levin, C. & Ravelli, R. B. G. (2002). *J. Synchrotron Rad.* **9**, 342–346.

Weik, M., Ravelli, R. B. G., Kryger, G., McSweeney, S., Raves, M. L., Harel, M., Gros, P., Silman, I., Kroon, J. & Sussman, J. L. (2000). *Proc. Natl Acad. Sci. USA*, **97**, 623–628.

Weik, M., Ravelli, R. B. G., Silman, I., Sussman, J. L., Gros, P. & Kroon, J. (2001). *Protein Sci.* **10**, 1953–1961.

Yano, J., Kern, J., Irrgang, K.-D., Latimer, M. J., Bergmann, U., Glatzel, P., Pushkar, Y., Biesiadka, J., Loll, B., Sauer, K., Messinger, J., Zouni, A. & Yachandra, V. K. (2005). *Proc. Natl Acad. Sci. USA*, **102**, 12047–12052.

Yano, J., Kern, J., Sauer, K., Latimer, M. J., Pushkar, Y., Beisiadka, J., Loll, B., Saenger, W., Messinger, J., Zouni, A. & Yachandra, V. K. (2006). *Science*, **314**, 821–825.

Yoo, S. J., Angove, H. C., Burgess, B. K., Hendrich, M. P. & Münck, E. (1999). *J. Am. Chem. Soc.* **121**, 2534–2545.

Yoo, S. J., Meyer, J. & Münck, E. (1999). *J. Am. Chem. Soc.* **121**, 10450–10451.